Growth-Controlled Broad Emission in Phase-Pure Two-Dimensional Hybrid Perovskite Films

*Rhiannon M. Kennard, [†] Clayton J. Dahlman, [†] Juil Chung, [†] Benjamin L. Cotts, [#] Alexander A. Mikhailovsky, [+] Lingling Mao, [†] Ryan A. DeCrescent, [‡] Kevin H. Stone, [▪] Naveen R. Venkatesan, [†] Yahya Mohtashami, [‖] Sepanta Assadi, [‖] Alberto Salleo, [#] Jon A. Schuller, [‖] Ram Seshadri, [†+] and Michael L. Chabinyc. [†]**

† Materials Department, University of California, Santa Barbara, CA 93106, United States

‡ Department of Physics, University of California, Santa Barbara, CA 93106, United States

‖ Department of Electrical and Computer Engineering, University of California, Santa Barbara, CA 93106, United States

+Department of Chemistry and Biochemistry, University of California, Santa Barbara, CA 93106, United States

▪ SSRL, SLAC National Accelerator Laboratory, Menlo Park, CA 94025, USA.

Department of Materials Science and Engineering, Stanford University, 496 Lomita Mall, Suite 102, Stanford, CA 94305, United States

Corresponding Author

*Corresponding Author: mchabinyc@engineering.ucsb.edu

ABSTRACT.

Two-dimensional hybrid metal halide perovskites (2D perovskites) are attractive for light emitting devices, and other applications, because their emission is tunable across the visible spectrum. The emission profile of 2D perovskites can be broadened via a variety of mechanisms, and is further complicated by the presence of impurities. Here, the challenge of making phase-pure films in Ruddlesden-Popper phases ($(A')_2(A)_{n-1}B_nX_{3n+1}$ structure) is overcome by using a single A/A'-site cation, ethylammonium (EA), whose optimal size also prohibits formation of off-target phases. In the $(EA)_2(EA)_{n-1}Pb_nBr_{3n+1}$ family, the low-energy, broad emission observed in bulk crystals is reduced in spin-cast, polycrystalline films. This decrease in broad emission, attributed to phonon-mediated processes, is correlated with strain in polycrystalline films that is observed by X-ray scattering. Photothermal deflection spectroscopy shows that strain also increases electronic disorder near the free exciton absorbance. Broad emission in films can be recovered by slowing growth kinetics, which removes the strain acquired from spin-casting and increases domain size. These results help extend the utility of 2D perovskites by providing design rules for how to grow films with the targeted phase and emission.

INTRODUCTION.

Two-dimensional hybrid perovskites are attractive for optoelectronic applications such as solar cells and light-emitting devices because their optical emission can be controllably changed by their structure. [1–5] Many 2D perovskites belong to the Ruddlesden-Popper (RP) family, which has a layered $(A')_2(A)_{n-1}B_nX_{3n+1}$ structure, where A' and A are cations, B is a divalent metal and X is a halide. [4–10] By changing the number *n* of B-X octahedral sheets that sit between large, organic A' cations (called spacer cations), the energies of the band gap and the free exciton shift, leading to tunable emission across the entire visible spectrum. Increasing distortions in B-X octahedral bond lengths and angles has been found to broaden the emission, with some compounds emitting white light.[11–17] This broad emission has been proposed to originate from radiative recombination of self-trapped excitons (STEs).[11–15,17–21] The detailed mechanism(s) of broad emission are under debate, however, and include different types of STEs,[17,18,22] coupling of STEs to specific point defects, [16] coupling of phonons to spacer cation stacking,[23] phonon replicas,[24] polaron self-localization,[25] extrinsic effects,[26,27] and shallow traps.[28] Because of the potential applications of 2D perovskites, understanding the impact of structure on optical properties continues to be an important goal.

Because perovskite optoelectronic devices typically comprise polycrystalline thin films, [3,29–34] much work has been devoted to determining how the growth of RP phases in polycrystalline form affects optical properties. RP phases with narrow emission (i.e., free exciton emission) exhibit similar spectral features in single crystals and in phase-pure polycrystalline thin films. [9,35,36] Strain, which is typically present in films, [37–42] results in a small energy shift in the free exciton emission. [43] The growth conditions used to cast films of RP-phases can produce impurities, which are typically higher-*n* RP phases and 3D phases, that cause the emission to red-shift relative to that of the intended phase. [44–50] However, being able to tune the emission color of RP-based LEDS or

lasers requires elimination of the undesired, higher-*n* RP phases and 3D phases.[34,45,46,51–53] Many attempts have been made to control the phase composition of RP films, and include changing the annealing procedures, the growth kinetics, the stoichiometry of the precursors, the solvent, and introducing additives to the precursor solution.[35,44,48,49,54–61] While recent work has achieved growth of phase-pure RP films with narrow emission,[36] less is known about growing polycrystalline films of broad/white emitting perovskites. In particular, the impacts of growth conditions on the optical properties of broad-emitting, 2D perovskites are not yet understood.

Here, we find that film growth can greatly affect the proportions of broad vs. narrow luminescence emitted by a solution-cast 2D phase. We found that using a single A/A'-site cation, ethylammonium (EA), enables spin-casting of phase-pure RP films of $(EA)_2(EA)_2Pb_3Br_{10}$. The optimal size of this cation also prohibits off-target phase formation due to unfavorable tolerance factor and octahedral distortions. Strain that occurs in thin films favors high-energy, narrow emission. In contrast, slowing the growth kinetics and removing strains encourages broad, lower-energy emission. Lower-energy emission appears to be phonon-coupled, and can be attributed to self-trapped exciton emission or to phonon replicas.

EXPERIMENTAL SECTION.

Materials Lead bromide ($PbBr_2$, 99.999 %), ethylammonium bromide (EABr, ≥ 98 %), lead oxide (PbO, ≥ 99.0 %), N-N-dimethylformamide (DMF, 99.8%, anhydrous), poly (methyl methacrylate) (PMMA, molecular weight 350000), and hydrobromic acid (HBr, ACS reagent, 48%) were purchased from Sigma Aldrich and used as received. Polished z-cut quartz substrates (15 × 15 × 0.5 mm) were purchased from University Wafer.

Film casting Quartz substrates were cleaned via ultrasonication in isopropyl alcohol for 10 min and exposed to oxygen plasma at ≈ 300 mTorr for 10 min. All subsequent solution preparation and film fabrications were performed in a nitrogen-filled glove box. Precursor solutions for $(EA)_2(EA)_2Pb_3Br_{10}$ were fabricated by dissolving 0.375 mmol (47 mg) EABr and 0.25 mmol (92 mg) $PbBr_2$ (molar ratio of EA/Pb = 1.5) in 0.5 mL DMF, to make an 0.5 mM solution (based on Pb). To make other compositions ($(EA)_2PbBr_4$ and mixed-phase films), the ratio of EABr/ $PbBr_2$ was adjusted following **Figure S18**. The solutions were left stirring overnight at 60°C to ensure good dissolution. Films were spin-cast at 4000 rpm for 60 seconds without antisolvent rinse, and promptly annealed at 100°C (verified by thermocouple) on a hot plate with a heat diffuser. After the films cooled, 60 μL of a PMMA solution (75 mg PMMA in 3 mL toluene) was spin-cast on top of the films at 2000 rpm for 30 seconds. The films were stored in a nitrogen glove box until characterization. For SEM, PDS, and certain stability experiments, the same spin-casting procedures were employed, but PMMA was not cast on the films. Films for PDS were cast on separate amorphous quartz substates.

Growth of $(EA)_4Pb_3Br_{10}$ bulk crystals $(EA)_2(EA)_2Pb_3Br_{10}$ bulk crystals were grown similarly to the previously-published procedure. [12] Briefly, PbO and EABr (in 3:4 molar ratio) were dissolved in HBr, and the solution was heated. Large crystals of $(EA)_2(EA)_2Pb_3Br_{10}$ formed upon cooling.

GIWAXS characterization. Grazing Incidence Wide-Angle X-Ray Scattering (GIWAXS) experiments were performed on beamline 11-3 (12.7 keV, wiggler side-station) at the Stanford Synchrotron Radiation Lightsource (SSRL). The source-to-detector (two-dimensional Rayonix MX225 CCD) distances were calibrated using lanthanum hexaboride (LaB6). All raw images were geometrically corrected using Nika. Au nanoparticles (100 nm) drop-cast on quartz substrates were used to verify chi-q alignment during post-processing. Sections (cakeslices) of the 2D GIWAXS

patterns at specific angles were selected and integrated to obtain 1D patterns (see **Figure S4**). The two cakeslices used were near-out-of-plane ("nOP", 3°-21°) and near-in-plane ("nIP", 70°-88°), both with a chi-q angle width of 18°. An incidence angle of 0.5° was chosen for the following reasons: (1) it is shallow enough to properly detect the nIP ($0k0$) peaks (these were cut off when large incidence angles, such as 2°, were used) and (2) it is well above the critical angle. The critical angle was calculated to be near 0.17° using GIXA; [62] this value is slightly below the measured critical angles (0.2°-0.26°) of similar 2D hybrid perovskites. [63] It is important to be far enough above the critical angle to avoid double diffraction, which may manifest in the nOP (but not nIP) peaks. [64] All peaks were fit to Pseudo-Voigt patterns using Igor, with Gaussian and Lorentzian contributions kept constant (Igor Multipeak "shape" factor of 1) across all peaks.

PDS characterization Photothermal Deflection Spectroscopy (PDS) measurements were performed using a homebuilt instrument as previously described. [65] Briefly, monochromated light from either a 150 W Xenon or a 100 W halogen lamp was modulated at 0.5 Hz with a mechanical chopper and then split to be separately focused onto the sample and a pyroelectric detector. Degassed and filtered perfluorohexane (C6F14, 3M Fluorinert FC-72) was employed as the deflection medium. The deflection of a HeNe laser aligned perpendicularly to the pump beam to also be parallel and proximal to the sample surface was measured by a position-sensitive Si detector using a lock-in amplifier. Analysis and fitting were performed using MATLAB. Absorbance peak positions are best determined from UV-Vis (**Figure 3a**), since the PDS signal is less accurate above 3 eV.

Powder X-Ray Diffraction patterns were obtained using a Panalytical Empyrean powder diffractometer in reflection mode with a Cu-Kα source, operating with an accelerating voltage of 45 kV and beam current of 40 mA. Au nanoparticles (100 nm) drop-cast on quartz substrates were

used to calibrate peak positions for strain characterization. All peak locations were obtained by Pseudo-Voigt fits using Igor Pro 8.

Plotting X-Ray crystal structures VESTA software was used to plot the CIF files of $(EA)_4Pb_3Br_{10}$ and $(EA)_2PbBr_4$, which were determined in prior work. [12,13] Color schemes for the octahedra and ions were modified, to highlight patterns in octahedral distortions. Bond lengths and angles were also measured using VESTA.

Scanning Electron Microscopy was performed using an FEI Nova Nano 650 FEG SEM operating at 7-10 keV accelerating voltage with beam currents of 0.40-0.80 nA. For SEM measurements, the samples were sputter-coated with gold to prevent charging.

Absorbance spectra were extracted from transmission measurements made on a Shimadzu UV-2600 ultraviolet-visible spectrophotometer at room temperature and in ambient conditions.

Photoluminescence spectra were acquired using a Horiba FluoroMax 4 spectrometer (i.e., fluorimeter) calibrated with Milli-Q water. The fluorimeter's excitation source was a 150 W xenon, continuous output, ozone-free lamp; the excitation energy was obtained using a monochromator. The detector was a PMT, also equipped with a monochromator. Photoluminescence spectra reported in in the main text were all collected using an angle of 75° between the excitation and emission port to reduce scattering. Some PL spectra in the SI (**Figures S1**, **S8**) were acquired using an angle of 25° for comparison, since the proportions of different features can be angle dependent. [18,22] All measurements were performed with an excitation wavelength of 370 nm (3.35 eV). A 400 nm long-pass filter was placed in front of the mission port to reduce scattering. Spectra were fit to Gaussians using Igor Pro 8.

Temperature-Dependent Photoluminescence measurements were performed using a home-build photoluminescence spectrometer. For the temperature control, the samples were placed into a LN2-cooled cold finger cryostat (Janice VPF-100) with Lakeshore 335 temperature controller. An 80 MHz laser pulse train with wavelength of 370 nm (3.35 eV) was used as the excitation source; the pulse energy was in sub 100 pJ range and the diameter of the laser spot was about 100 μm. The UV laser light was produced by frequency doubling the output of Spectraphysics Tsunami Ti: Sapphire femtosecond laser oscillator with the fundamental wavelength of 740 nm in Coherent/Inrad optical harmonics generator. We verified that at the given laser energy density level there was no photoinduced damage to the sample, as the PL spectra did not change over time under continuous laser illumination. The PL emission was collected in near 90 degrees geometry by a system of lenses and focused on the input slit of a spectrometer (Acton Research SP500). The stray laser light was blocked by an interference long pass filter (Omega Filters) with cut on wavelength 380 nm. The spectra dispersed by the spectrometer were recorded by a charge-coupled device detector (Princeton Instruments PIXIS:400). The spectra collected were corrected for the instrument response by measuring the response of the setup to the light of a black body-like source (Ocean Optics LS-1) and calculating appropriate correction factors. All spectra were fit to Gaussians using Igor Pro 8.

RESULTS AND DISCUSSION.

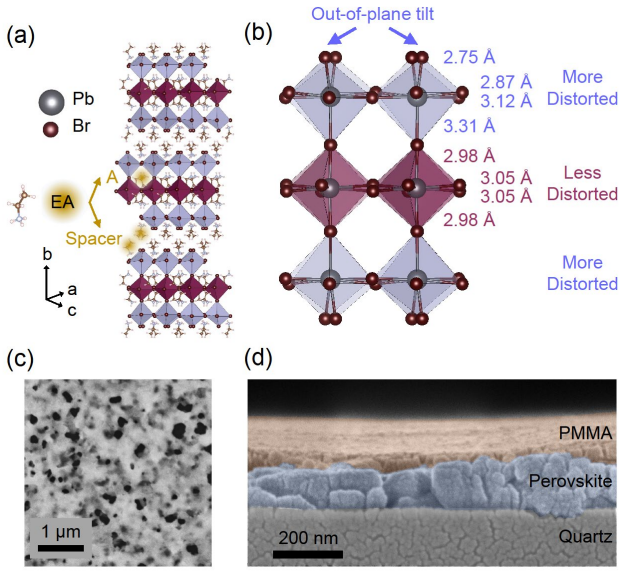

Figure 1. (a) Crystal structure of $(EA)_4Pb_3Br_{10}$ with (b) Pb-Br bond lengths and octahedral distortions. (c) Top-view and (d) cross-sectional SEM images of an $(EA)_4Pb_3Br_{10}$ film spin-cast on quartz. Films were capped with PMMA for most measurements, but not for top-view SEM. The black color in the background of (c) is the substrate.

We aimed to understand relationships between growth and optical properties in polycrystalline thin films of RP phases that exhibit broad emission. One challenge encountered during the growth of films of RPs phases with $n > 1$, is that the A-site and A'-site (spacer) cations can segregate into different phases, resulting in highly-emissive 3D impurities.[48] To circumvent this challenge, we sought to study the growth of RP phases in which A and A' are identical. We therefore selected the $(EA)_2(EA)_{n-1}Pb_nBr_{3n+1}$ family, where EA is ethylammonium. The structures of the $n = 1$ and $n = 3$ phases of this family have been determined from bulk crystals. [12,13] The $n = 1$ phase contains single sheets of Pb-Br octahedra separated by EA cations (**Figure S1**). The structure of the $n = 3$ phase, $(EA)_4Pb_3Br_{10}$, [12] is shown in **Figure 1**. To accommodate the large size of EA in the A-site (274 pm), [66,67] the 3-layer inorganic sheet forms two substructures, comprising highly-distorted

outer octahedra and relatively undistorted inner octahedra (**Figure 1b**). The bond lengths of the outer, distorted octahedra show large variations (≈ 20 %), with the shortest at 2.75 Å and the longest at 3.31 Å, while those of the inner octahedra have less variation. The outer layers also exhibit significant out-of-plane tilting, contrary to the inner octahedra. The angle and bond length [11–17] distortions in the outer layers are thought to encourage formation of self-trapped excitons (STEs), which create broad, lower-energy photoluminescence.[12,16] Both the $n = 1$ and $n = 3$ phases of the $(EA)_2(EA)_{n-1}Pb_nBr_{3n+1}$ family exhibit pronounced narrow emission from free excitons, as well as broad emission at room temperature.[12,13] Thus, studying the properties of $(EA)_2(EA)_{n-1}Pb_nBr_{3n+1}$ films can reveal if strain and growth kinetics impact emission.

We first verified the phase composition of $n = 3$ and $n = 1$ $(EA)_2(EA)_{n-1}Pb_nBr_{3n+1}$ films before assessing how growth conditions impact optical emission. To prepare films of $n = 3$, we spun-cast precursor salts in nearly-stoichiometric proportions (see **Experimental Section**). A very small excess of EA was found to be necessary to grow the films, likely counteracting strong Pb-Br-DMF complexation. [68] Films were then capped with PMMA to prevent possible degradation. The as-cast $n = 3$ films exhibit ≤ 200 nm domain size and thickness and many pinholes (**Figure 1c-d**). Bulk crystals of $n = 3$ were grown using literature methods [12] and the crystal structure was verified (see **Experimental Section** and **Figure S2**). We also prepared $n = 1$ films and confirmed their composition for comparison with the $n = 3$ films (**Figure S1**).

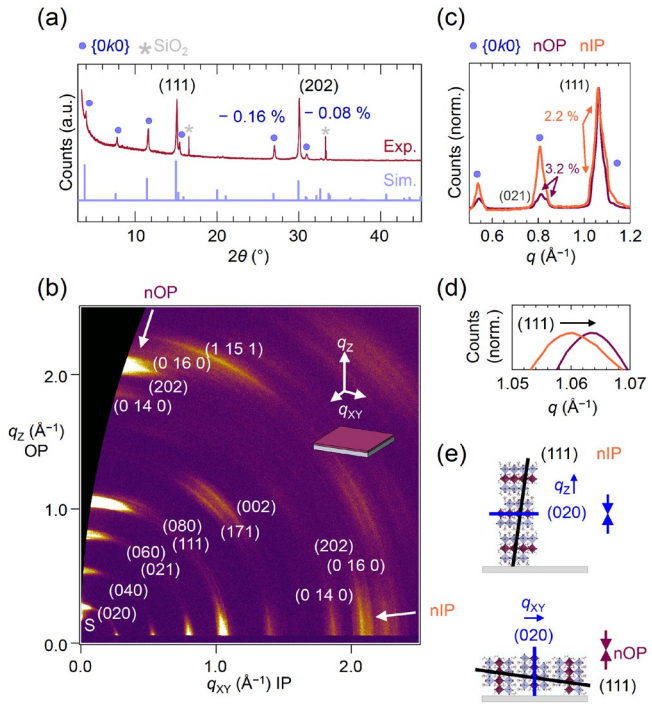

Figure 2. (a) XRD pattern of a spin-cast $(EA)_4Pb_3Br_{10}$ film, with % strain labeled for $(EA)_4Pb_3Br_{10}$ peaks, and a simulated (Sim.) powder pattern assuming no preferred crystallite orientation. (b) Grazing Incidence Wide-Angle X-Ray Scattering (GIWAXS) pattern of a spin-cast $(EA)_4Pb_3Br_{10}$ film expressed as a function of the scattering vector, $q = 4\pi\sin(2\theta/2)/\lambda$, where λ is the X-Ray wavelength. The near-out-of-plane (nOP) and near-in-plane (nIP) regions are indicated and peaks are indexed by the bulk crystal structure. S indicates spillover from the incident beam. (c) Integrated and normalized nOP and nIP patterns, with *relative* % strain of select peaks. (d) Inset of (c), showing a closer view of the (111) nOP and nIP peak positions. (e) Schematic of the two primary crystallite orientations identified from the GIWAXS pattern: one oriented with (0*k*0) in-plane (q_{XY} axis) and the other oriented with (0*k*0) out-of-plane (q_Z axis). Out-of-plane-oriented peaks have mild compressive strain: (111) nOP is more compressed than for the in-plane-oriented crystallites.

X-ray scattering from the as-prepared $n = 3$ films is consistent with the desired $(EA)_4Pb_3Br_{10}$ phase (**Figure 2**). The X-Ray diffraction (XRD) pattern of the $n = 3$ film is in good agreement with the simulated powder pattern of this material (**Figure 2a**). Peaks corresponding to the $(EA)_4Pb_3Br_{10}$ phase were present, and the only peaks missing (near 20°, corresponding to (171) and (002)) were off-specular peaks that were later observed via GIWAXS (**Figure 2b**). In the XRD pattern, (**Figure 2a**), the (0*k*0) and (111) features have approximately the relative intensities that would be expected from the simulated XRD pattern of the single crystal structure. [12] The presence

of (0*k*0) features suggests phase purity, since they appear strongly in phase-pure RP films [36] and in powders of the targeted RP *n* phase. [9] In contrast, the (0*k*0) are weakened relative to other peaks, or absent entirely, in mixed-phase films [45] due to stacking fault defects that result in intergrowth of different *n* within a single grain. [45,46] Grazing Incidence Wide-Angle X-Ray Scattering (GIWAXS) patterns of the films were collected to probe off-specular diffraction (**Figure 2b**). All observed peaks are indexed to features of $(EA)_4Pb_3Br_{10}$ (**Figure S3**) with the only missing peaks predicted to have very small intensity. GIWAXS confirms that there is a distribution of orientations of crystallites in the films (**Figure 2b**). In particular, the presence of (0*k*0) and (111) *only* near q_{XY} and q_Z, but not in between, reveals that the Pb-Br octahedral sheets prefer to grow either parallel or perpendicular to the substate (**Figure 2c-d**). Further analysis reveals a slight preference for the crystallites growing with Pb-Br octahedra growing perpendicular to the substrate (**Figure S3**). Thus, the $(EA)_4Pb_3Br_{10}$ films appear phase-pure and textured based on X-ray scattering.

X-ray scattering also reveals that the crystallites in the $n = 3$ films exhibit strain. Based on the peak shifts seen in XRD (see **Experimental Section**), the film is compressively strained (by under 0.3 %) in the out-of-plane direction (**Figure 2a**). This mild strain is consistent with prior reports of the spin-coating [38] and/or annealing [37] procedures imparting mild biaxial stress in hybrid organic metal halides. To examine strain in greater detail, sections of the GIWAXS pattern were integrated near-out-of-plane (nOP) and near-in-plane (nIP) (see **Figure S4** for definition of these areas), and normalized for clarity. The position of the (111) nOP is shifted into compression, in agreement with the mild compression observed in XRD, and is additionally more compressed than the (111) nIP (**Figure 2a/c/d**). The difference in strain between the (111) nOP and (111) nIP shows that the mild biaxial strain affects out-of-plane vs. in-plane oriented crystallites differently (**Figure 2d**). In addition, small peaks are identified near the main (0*k*0) and (111) peaks for the nOP and nIP

patterns (**Figure 2d** and **Figure S4**), and are assigned to strained (0*k*0) and (111) features. From peak fits, these weaker peaks have 2-3 % strain relative to their respective main (0*k*0) and (111) peaks. Overall, the films exhibit mild biaxial strain that differently affects in-plane vs. out-of-plane oriented crystallites, with small populations of highly-strained crystallites.

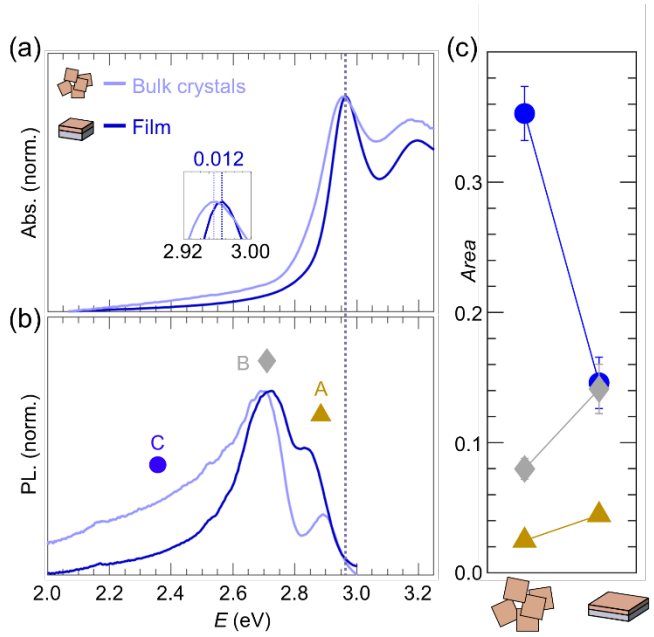

Figure 3. (a) Absorbance and (b) Photoluminescence (excitation 3.35 eV) of bulk crystals and spin-cast films of $(EA)_4Pb_3Br_{10}$. The inset in (a) shows the energy difference between the n = 3 free exciton peak of the bulk crystals and film. The dashed line connecting (a) and (b) is a guide to the eye. Emission peaks are labelled A, B and C. (c) Gaussian area of features A, B, and C (see **Figure S5** for fits and "Fitting the Photoluminescence Data" and "Temperature-Dependent PL" sections in the **Supporting Information** for fit methodology).

The optical properties of polycrystalline films and bulk crystals of $(EA)_4Pb_3Br_{10}$ show features of only n = 3. The UV-Vis absorbance spectra of polycrystalline thin films and bulk crystals (**Figure 3a**) are both in agreement with the previously reported spectrum of bulk crystals. [12] The absorbance spectra of the bulk crystals and film exhibit a sharp increase near the main n = 3 excitonic feature at ≈ 3.0 eV (**Figure 3a**). In contrast, thin films of n = 3 RP phases that also contain off-target n or 3D impurities frequently show absorbance spectra that have large sub-gap slopes

and poorly-visible $n = 3$ excitonic features.[45,48,53,63,69] For both films and crystals, the 2.9 eV onset of emission is close in energy to the absorbance onset (dashed line in **Figure 3**), which is a sign of phase purity. If lower band-gap phases were present, even in small concentrations, we would expect emission from excitations funneled to these phases, as observed in mixed-phase $(BA)_2(MA)_{n-1}Pb_nI_{3n+1}$ RP films.[45,48] Three primary features are observed in the emission of bulk crystals and films: a high-energy excitonic feature near 2.9 eV (peak A), one near 2.7 eV (peak B), and broad emission below 2.7 eV (peak C - for spectra in nm, see **Figure S6** [70]). No other emissive features are detected. Thus, the optical properties of the films are those of the $n = 3$ phase.

The proportions of the different $n = 3$ emission peaks change considerably from bulk crystals to films (**Figure 3b**). To better assess these changes, we fit the normalized emission spectra (**Figure S5**) and examined the areas of peaks A, B and C (**Figure 3c**). The integrated area of the free exciton at 2.9 eV (peak A) does not change much from bulk crystals to films. However, the area of B (2.7 eV) increased slightly in films, which is the opposite of what is seen from self-absorption, as peaks from self-absorption become weaker in thinner perovskites. [71] Notably, the broad, low-energy tail, C, decreases sharply in area from bulk crystals to polycrystalline films. Broad, low-energy peaks that are far in energy from the free exciton, such as C, are commonly attributed to self-trapped excitons [11–17] and not to self-absorption.[71] To further understand the origin of feature C, we excited bulk crystals below-gap (2.75 eV), and observed no emission (**Figure S7**). Thus, C does not come from impurities or extrinsic effects[26] and $(EA)_4Pb_3Br_{10}$ must be excited above-gap for the low-energy emission (peak C) to appear, which is again consistent with attributions of peak C to self-trapped excitons.[11–18] We then confirmed that the changes in relative areas of A, B and C were not due to measurement conditions (see **Figure S8**-**S9**), since the proportions of emissive features in 2D materials can sometimes vary with collection angle. [18] In all cases, the bulk $n = 3$ crystals

exhibit more low-energy tail emission (peak C) than the polycrystalline films. We also notice that the EA n = 1 films contain the same emission features as bulk n = 1 crystals, but proportionally less low-energy, broad emission than that reported for the bulk n = 1 crystals (**Figure S1**). [13] Thus, the targeted-n emission seems to be preserved in films for both n = 3 and n = 1, but with large changes to the proportions of emissive species.

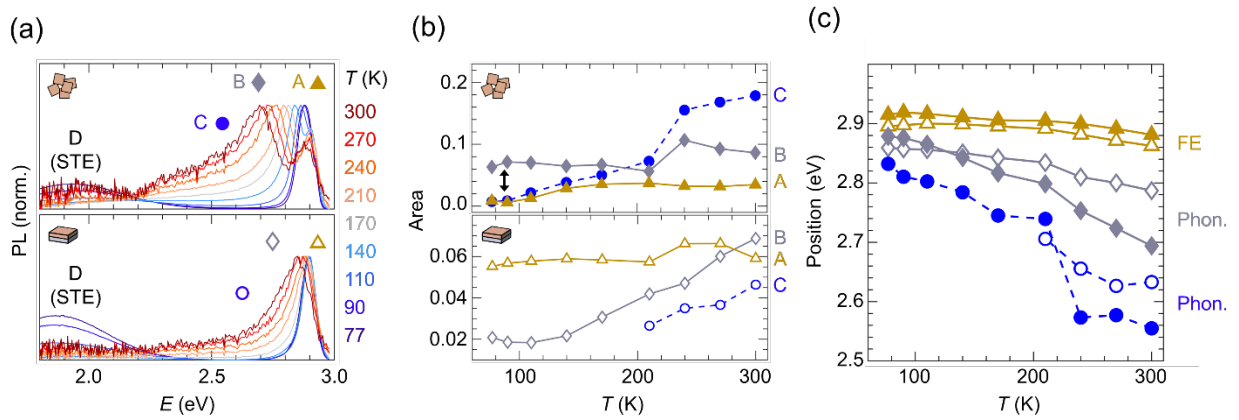

Figure 4. Effects of cooling on photoluminescence. (a) Temperature-dependent photoluminescence of bulk crystals (top panel) and film (bottom panel) of $(EA)_4Pb_3Br_{10}$, with pulsed excitation at 3.35 eV (see **Experimental Section**). Peak D is likely an STE (**Figure S15**). (b) Evolution of integrated area of peaks A, B and C with temperature for bulk crystals (top panel) and a film (bottom panel). For discussion of fits, see **Figures S10-S15**. The black arrow indicates strong overlap between peaks A and B at low temperatures in the bulk crystals, making decoupling A and B difficult at low temperatures. (c) Evolution of peak position with temperature for peaks A, B, and C in the bulk crystals and films. FE stands for free exciton and Phon. for phonon-coupled.

Temperature-dependent emission reveals several types of emission features, which allows us to understand the changes in emission proportions in films (**Figure 4**). The normalized emission spectra with cooling of bulk crystals and films are shown in **Figure 4a**, with peak area (**Figure 4b**) and peak position (**Figure 4c),** and fits in **Figure S10** and **S15**. Similarly to other compounds, [14,17,20,21,25] a broad peak appears at 110 K near 1.9 eV in both bulk crystals and films (peak D). In agreement with the behavior of certain STEs observed in perovskites, [14,17,20,21,25] peak D is located at much lower energies than the free exciton and its intensity steadily increases with cooling

(**Figure S11**). This increase is attributed to less de-trapping back to the free exciton state at lower temperatures, [17,25] which here happens near 110 K (**Figure S15**). Like B and C, D has different proportions in bulk crystals and in films (**Figure 4**, **S15**); D is stronger in films, suggesting that it has different nature from B and C. Indeed, a red-shift of peak D is observed with cooling for the bulk crystals, consistent with polaron localization of the carriers (**Figure S15**). [25] In contrast, B and C blue-shift strongly with cooling, and C seems to disappear at low temperatures. The blue-shift of B with cooling is readily visible in **Figure 4** and we examined different fitting methods to quantify the blue-shift and the disappearance of C (**Figures S10** to **S14**). It is possible that B and C blue-shift so strongly with cooling that they overlap with themselves or with peak A, as highlighted by the black arrow in **Figure 4b**. The large blue-shift/disappearance of B and C with cooling is consistent with coupling to phonons, as similar blue-shifts have been previously observed in the phonon-coupled features of $(A')_2PbI_4$ [18,24] and lithium niobate. [72] In particular, the energy shifts with cooling of C (277 meV in the crystals) and B (184 meV in the crystals; 72 meV in the film) are on the order of the blue-shifts observed in $(A')_2PbI_4$ (50-120 meV) over a similar temperature differential. [18,24] The strongly blue-shifting feature of $(A')_2PbI_4$ has been assigned to an STE with specific phonon-coupling behavior [18] and separately to a phonon replica; [24] both are possibilities for B and C. This large blue-shift/disappearance with cooling of B and C contrasts with the reported behavior of extrinsic features, [26] polaron self-localization, [25] convolutions of a bright exciton with a localized state, [28] or shallow traps, [28] as these have different behavior with cooling (e.g. red-shifts or increases in intensity). Self-absorption is also ruled out, as the blue-shifts of B and C are larger (>10x) than shifts expected from self-absorption. [71] In addition, the free exciton (peak A) exhibits a smaller shift with cooling (34 meV and 33 meV in crystals/films respectively) than B and C, consistent with previously-reported free exciton behavior. [18,24] Overall,

the behavior of B and C is most consistent with phonon-mediated processes, such as STEs or phonon replicas, and D is a more commonly-observed STE.

Strain likely causes the differences in the proportions of emission from A, B, C, and D in bulk crystals and polycrystalline films (**Figures 2, 3, 4**). Film strain observed in the $(EA)_4Pb_3Br_{10}$ films by X-ray scattering (**Figure 2**) is likely the origin of the small blue-shift (by 0.012 eV) of the main free exciton in the film compared to that in bulk crystals (**Figure 3**). Similar shifts (≈ 0.013 eV) in free exciton energy were observed in other 2D perovskites upon application of ≈1 % strain.[43] Strain can also affect the lower-energy emission: prior work on bulk crystals of $(BA)_2PbBr_4$ found that microstrain, caused by different stackings of spacer cations in the bulk region, may enhance emission that is lower-energy and phonon-coupled.[23] Given that B and C exhibit phonon-coupled behavior and that the crystallites are strained (**Figure 2**), it is likely that changes to the emission intensities of B and C are linked to these strains. We would not expect such changes to result from differences in domain size, as major changes to electron-phonon coupling occur on much smaller size scales (≤ 20 nm) [73,74] than those of our experiment (≤ 200 nm). Experimentally decoupling the effects of thickness or domain size is not so easy, as preparing thinner samples involves either spin-casting or mechanical exfoliation, and both of these may lead to imposition of strain. [38] We exfoliated bulk crystals of $(EA)_4Pb_3Br_{10}$; the results are consistent with different strain changing the relative proportions of B and C (see discussion of **Figure S5**). Furthermore, in 1-D or 0-D hybrid halide perovskite-like free-standing crystals, strain has also been found to turn the emission from STEs off or on, depending on whether strain decreases or increases Pb-Br octahedral distortions. [11,75] In particular, when strain decreased the octahedral distortions, [11] the free exciton emission (narrow and higher energy) proportionally increased at the expense of the STE emission. Here, we find that the films contain strain that varied between 0.1 % and 3 % (**Figure 2**), which is

on the order of the deformation that were found to decrease STE emission in free-standing, micron-sized crystals under pressure [11] (see "Further Explanations regarding Strain" in the **Supporting Information** [76,77]). The changes in emission intensity of B, C and D from bulk crystals to polycrystalline films thus likely stem from film strain, which can affect both spacer cation stacking and octahedral distortions.

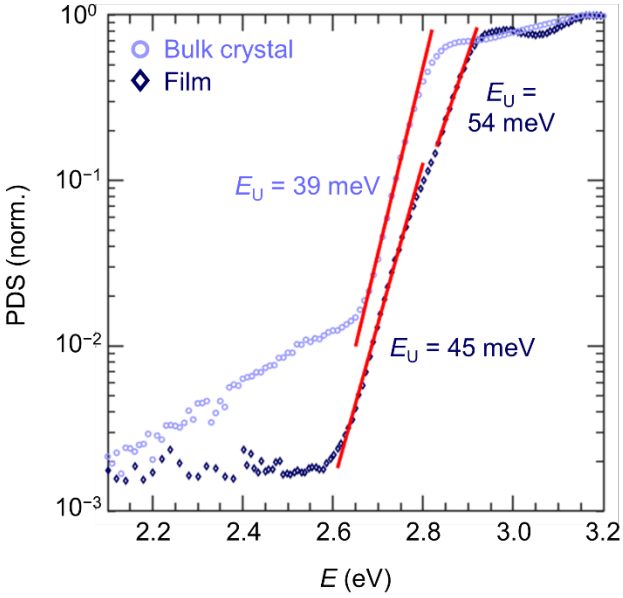

Figure 5. PDS spectra of a bulk crystal and film of $(EA)_4Pb_3Br_{10}$, showing fits of different absorption onsets (see **Supporting Information** - "Fitting the PDS Data") and the extracted Urbach energies E_U. More detail in the 2.6 eV-3.0 eV region, as well as goodness of fits, are shown in **Figure S16**.

Photothermal Deflection Spectroscopy (PDS) was then used to examine more subtle optical changes caused by switching from bulk crystals to polycrystalline films (**Figure 5**). PDS enabled highly sensitive measurement of the absorption onsets throughout the film thickness (see **Experimental Section**). The slight blue-shift of the film's PDS absorbance with respect to that of bulk crystal is consistent with the UV-Vis measurement of **Figure 3a** (see also **Experimental Section**). The lack of any PDS absorbance feature in the film below the main onset is further indication of $n = 3$ phase purity in the films. In contrast, nominally $n = 3$ films with mixed-phase

composition exhibited low-energy absorbance features, that were indexed to higher-*n* Ruddlesden-Popper phases. [48] The bulk crystal of $(EA)_4Pb_3Br_{10}$ exhibits a tail at low energy, but this tail is non-emissive when excited directly (**Figure S7**), so we rule out emissive impurities or extrinsic effects [26] as the source of the tail. We fit portions of the PDS spectra (see **Experimental Section** and "Fitting the PDS Data" in the **Supporting Information**) to extract the Urbach energies E_U, representing the degree of disorder in electronic states near the absorption edge (see also **Figure S16**).

The differences in onset between the film and bulk crystal can be attributed to strain (**Figure 5**). While the bulk crystal only exhibits one absorbance onset with an Urbach energy E_U of 39 meV, the film exhibits two onsets that can be fit with different E_U of 45 meV and 54 meV. GIWAXS reveals populations of crystallites with two different strain states (**Figure 2**). The two absorbance onsets, with their two distinct Urbach energies, likely correspond to these two states because of the sensitivity of free excitons to strain. [43] The increase in Urbach energies from the crystal (39 meV) to the film (45 and 54 meV) also likely originates from strain. In addition, the weak, sub-gap absorbance in the bulk crystal below 2.6 eV is likely connected to the larger amount of broad, lower-energy emission from C in the bulk crystals. Direct excitation near the absorbance tail does not lead to emission (**Figure S7**), ruling out emissive impurities as the source of the tail. However, it is clear that making $(EA)_4Pb_3Br_{10}$ as a film prevents formation of this tail. Thus, strain has two effects: it can increase the electronic disorder of the free excitons present, and may hinder formation of sub-gap states in bulk samples. These results suggest the importance of controlling strain during growth of thin films for modifying the photoluminescence.

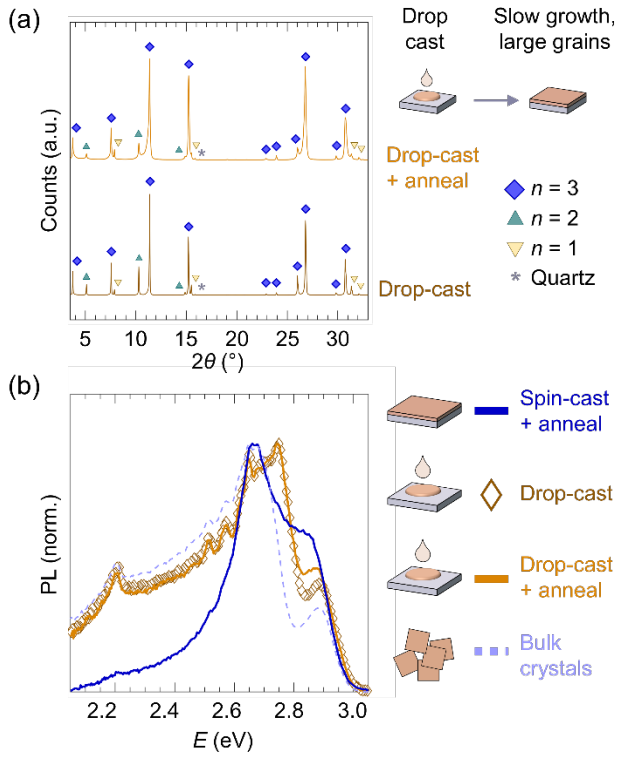

Figure 6. (a) XRD patterns of films made by drop-casting the n = 3 precursor solution, with/without annealing. (b) Photoluminescence of these films (3.94 eV excitation). The emission spectra of $(EA)_4Pb_3Br_{10}$ bulk crystals and spin-cast films are also shown.

Having examined the various ways in which film strain can impact the optical properties of $(EA)_4Pb_3Br_{10}$, we next sought ways to control the optical properties of films by controlling film growth. Film strains suggest that rapid spin-casting may not be the optimal growth method for controlling low-energy emission. Because film strains can originate from stresses acquired during spin-casting [38] and from thermal expansion mismatch between the material and substrate during annealing, [37] we tried to modify the deposition kinetics to avoid these two factors. We slowed the deposition kinetics by drop-casting the precursor solution and allowed the solvent to slowly evaporate (in N_2 atmosphere glove box for 1h). The samples were then, in some cases, annealed, and then capped with PMMA for protection (see **Experimental Section**). SEM images of the non-annealed and annealed films show large domains, ~20 μm-wide and ~3 μm-thick, without complete coverage of the substrate (**Figure S17**). Thus, in the drop-cast films, the domains grow

on the substrate with few spatial constrains from neighboring domains, in contrast to spin-cast films. The domains exhibit one crystal habit and are isotropic and homogeneous, suggesting that non-RP phases, such as solvates or other intermediates, do not form, in contrast to the behavior of other drop-cast 2D or 3D perovskites. [48,49,78] XRD patterns of drop-cast films, with and without annealing, are shown in **Figure 6a**. The drop-cast films contain in majority $n = 3$ and the positions of the peaks do not indicate strain. Additionally, small amounts of $n = 1$ and additional features are present. Because only $n = 1$ and $n = 3$ single crystal structures have been reported, we attribute the additional peaks to $n = 2$, by estimation of where the $n = 2$ peaks should be based on analogy with the $(BA)_2(MA)_{n-1}Pb_nX_{3n+1}$ RP peak locations. [9] These higher-n phases likely appear due to the slight excess of EABr used in the precursor solution, which was found necessary for spin-casting phase-pure $(EA)_4Pb_3Br_{10}$ films. To make all experiments self-consistent, we employed the same precursor solutions for spin-casting and drop-casting (see **Experimental Section**). Drop-cast films containing only $n = 3$ might be obtained in future studies by slightly modifying the EA: Pb precursor ratio.

Slowing growth by drop-casting enables recovery of the broad emission. **Figure 6b** shows the photoluminescence of the drop-cast films overlaid with those of the spin-cast $n = 3$ film and of the $n = 3$ bulk crystals. The drop-cast films exhibit comparable low-energy emission (peaks B and C) to the bulk crystals. An extra feature is observed near 2.75 eV, possibly originating from the small amount of proposed $n = 2$ in the drop-cast films (see **Figure 6a**). However, the spectra of the drop-cast films closely resemble that of the $n = 3$ bulk crystals, indicating that most of the emission comes from $n = 3$. Since domains in the drop-cast $n = 3$ films grow slowly and with few spatial constrains from neighboring domains, such slow and unconstrained growth of domains seems necessary for retaining the lower-energy emission. The $n = 3$ phase forms without thermal

annealing, and subsequent annealing does not lead to significant changes in emission. We note that mismatches between the thermal expansion coefficients of the substrate and film can lead to stresses in some cases. [37] Thus, overall, we find that deposition methods that reduce strain are likely to favor low-energy emission in films.

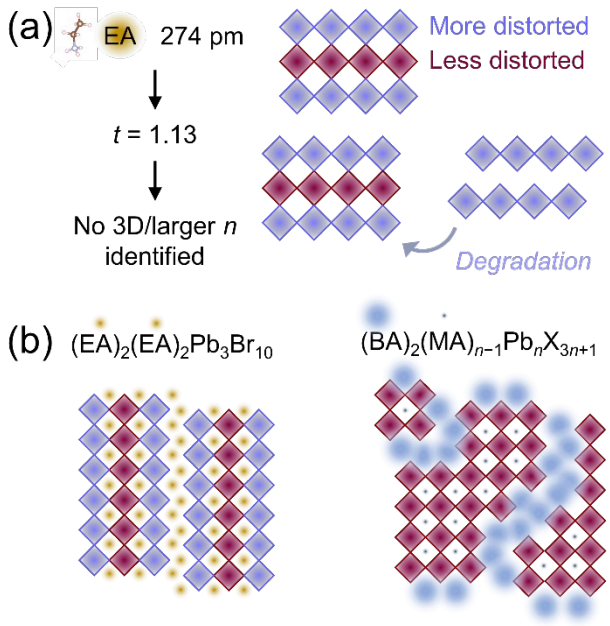

Figure 7. Origins of phase purity in the n = 3 films. (a) Summary of findings of **Figures 2**, **3**, **6**, **S18** and **S19**, where t stands for the tolerance factor. (b) Illustration of how stacking fault defects lead to intergrowth of n in the $(BA)_2(MA)_{n-1}Pb_nX_{3n+1}$ RP series, and how in contrast, the EA RPs lack different n phases available for intergrowth, resulting in n = 3 phase-purity.

Finally, we consider why only n = 3 is observed in spin-cast films, rather than other phases in the $(EA)_2(EA)_{n-1}Pb_nBr_{3n+1}$ family, and why it is favorably formed (**Figure 7**). The spin-casting procedures we used typically yield 2D-3D mixed-phase films unless particular care is taken, [36,45,46,48,49] so the formation of a phase-pure n = 3 film via spin-casting is notable. First, no experimental single crystal structure for a 3D $EAPbBr_3$ phase has been reported to our knowledge. Previous work that attempted to make films of 3D $EAPbBr_3$ found that a 2D phase formed instead,

[79] and we believe that prior assignments to the $EAPbBr_3$ phase in nanocrystals may actually correspond to $(EA)_4Pb_3Br_{10}$ (see "Further Discussion on 2D and 3D Phases" in the **Supporting Information**). [80] We also attempted to make $EAPbBr_3$ films (**Figure S18** and **Figure 7a**) and obtain non-emissive films with broad features in XRD. The absence of formation of a 3D perovskite phase of $EAPbBr_3$ is consistent with the tolerance factor for EA with Pb and Br prohibiting 3D phase formation (t = 1.13; see **Supporting Information - Methods** for calculation). By itself, EA (274 pm) [66,67] is just small enough to fit in the A-site of 2D phases, since the 2D perovskites have less strict requirements for tolerance factor. [81,82] The n = 3 and n = 1 RP phases in the $(EA)_2(EA)_{n-1}Pb_nBr_{3n+1}$ family have been reported as single crystal structures, [12,13] but there are no reports of phases with other n values. The phase purity observed in n = 3 and n = 1 films thus likely originates from lack of available other phases, due to the large size of EA, and consequently unfavorable tolerance factor for impurity 3D or larger-n RP phases. The presence of a single EA cation in the A/A' sites also limits the number of competing precipitations. This phase selectivity is in direct contrast to the behavior of the widely studied $(A')_2(A)_{n-1}Pb_n(I \text{ or } Br)_{3n+1}$ RPs families, where spin-casting leads to polycrystalline films with mixed RP and 3D phases, unless particular care is taken to suppress their formation. [34–36,44–46,48,49,51,52,54–61] For many RP compositions, the tolerance factor of the corresponding 3D structures, $MAPbI_3$ and $MAPbBr_3$, are 0.96 and 0.99 respectively, so a large variety of corner-sharing structures can form (**Figure 7b**) leading to more ready formation of off-target RP and 3D phases. [34,45,46,48,49,53] The ability to grow phase pure polycrystalline films with EA shows that selecting A-site cations that are too large to form 3D phases, but are within sizes tolerable for layered structures, is a route to eliminating alternative phase formation.

The $n = 3$ phase forms preferentially over the $n = 1$ phase, likely due to specific patterns of Pb-Br octahedral distortions (**Figure 7**). While the stoichiometry of the $n = 3$ precursor solution roughly matched $(EA)_4Pb_3Br_{10}$, a large excess of EA (nearly 2×) is needed to make thin films of $n = 1$ $(EA)_2PbBr_4$ (**Figure S18**). Synthesis of $n = 1$ bulk crystals is also reported to require EA excess, [13] unlike synthesis of $n = 3$ bulk crystals, which follows $n = 3$ stoichiometry. [12] In addition, not only are the $n = 3$ films much more stable to heat and the ambient than the $n = 1$ films, but the $n = 1$ films degrade to $n = 3$ (see discussion of **Figure S19**). Thus, $n = 3$ is much more easily formed and more stable than $n = 1$. This preference likely originates from the large size of EA (274 pm): [66,67] the $n = 3$ phase forms distorted/undistorted octahedral substructures within the Pb-Br sheets to accommodate this large size, and the less-distorted inner layer of the $n = 3$ likely stabilizes the 3-layer Pb-Br sheet. In contrast, the $n = 1$ contains phase only one highly-distorted octahedral layer (**Figure S1**). The $n = 1$ phase can thus can form in a phase-pure manner but requires significant stoichiometric excess to form (**Figure S18**) and readily transforms into the more stable $n = 3$ structure (**Figure S19**). We hypothesize that the $n = 2$ structure, similarly to the $n = 1$, would only contain highly distorted octahedral sheets, and not have the inner stabilizing layer of the $n = 3$ phase. Thus, the optimal size of the EA cation, creating the inner stabilizing layer and preventing 3D formation, is instrumental to casting phase-pure $n = 3$ RP films. Tailoring the ratio of less: more-distorted layers with cations other than EA may be crucial for spin-casting phase-pure RP films with $n \neq 3$.

CONCLUSIONS.

Overall, we find that that strain can greatly affect the relative proportions of different luminescence features emitted by a solution-cast 2D phase. Film strain can suppress lower-energy, broad emission that is coupled to phonons, in favor of free exciton emission. Film strain also

increases electronic disorder, and removes sub-gap absorbance features that are likely correlated with broad emission. Broad emission can be recovered by slowing the film growth and removing strain that arises from the fast growth during spin casting. This result suggests that growth methods that avoid rapid solvent removal, such as co-evaporation or blade coating, could prove more fruitful for retaining broad emission than spin-casting. For a given composition, strain should be characterized for the growth method chosen, to inform which method might be best. In addition, the use of a single cation (ethylammonium) for both the A-site and spacer of 2D perovskite phases enables casting of phase-pure films. The large size of this cation prevents 3D impurities from forming due to unfavorable tolerance factor, and prevents layered structures with other values of *n* from forming due to unfavorable octahedral distortions. These results further our understanding of how to control phase composition and emission in films, which extends the utility of 2D perovskites for light-emitting devices and may enable novel fabrication of perovskite-perovskite heterostructures, which are useful in a variety of devices.

ACKNOWLEDGMENT.

Growth and structural characterization were supported by the U.S. Department of Energy, Office of Science, Basic Energy Sciences, under Award Number DE-SC-0012541. Support of optical characterization was provided by the U.S. Department of Energy (DOE), Office of Science, Basic Energy Sciences (BES), under Award Number DE-SC0019273, as well as from Quantum Materials for Energy Efficient Neuromorphic Computing, an Energy Frontier Research Center funded by the U.S. Department of Energy (DOE), Office of Science, Basic Energy Sciences, (BES), under Award Number DE-SC0019273. Time-resolved spectroscopy capabilities were supported by DURIP ARO grant 66886LSRIP. Use of the Stanford Synchrotron Radiation

Lightsource, SLAC National Accelerator Laboratory, is supported by the U.S. Department of Energy, Office of Science, Office of Basic Energy Sciences under Contract No. DE-AC02-76SF00515. The research reported here also made use the shared facilities of the UCSB MRSEC (National Science Foundation DMR 1720256), a member of the Materials Research Facilities Network (www.mrfn.org). R.M.K. gratefully acknowledges the National Defense Science and Engineering Graduate fellowship for financial support.

ASSOCIATED CONTENT.

Supporting Information. Calculation of tolerance factors, further explanations regarding strain; additional data/fitting/comparison with simulations for photoluminescence/XRD/GIWAXS/PDS; additional SEM, precursor solution stoichiometry studies, film stability studies, further discussion on 2D and 3D phases with the EA cation (PDF), and further discussions of methods more generally.

AUTHOR INFORMATION.

Corresponding Author

Michael L. Chabinyc; Email: mchabinyc@engineering.ucsb.edu

Notes

The authors declare no competing financial interest.

REFERENCES

(1) Zhou, Y.; Chen, J.; Bakr, O. M.; Mohammed, O. F. Metal Halide Perovskites for X - Ray Imaging Scintillators and Detectors. *ACS Energy Lett.* **2021**, *6*, 739-768.

(2) Saparov, B.; Mitzi, D. B. Organic-Inorganic Perovskites: Structural Versatility for Functional Materials Design. *Chem. Rev.* **2016**, *116* (7), 4558-4596.

(3) Ge, C.; Xue, Y. Z. B.; Li, L.; Tang, B.; Hu, H. Recent Progress in 2D/3D Multidimensional Metal Halide Perovskites Solar Cells. *Front. Mater.* **2020**, *7*, 380.

(4) Li, X.; Hoffman, J. M.; Kanatzidis, M. G. The 2D Halide Perovskite Rulebook: How the Spacer Influences Everything from the Structure to Optoelectronic Device Efficiency. *Chem. Rev.* **2021**, *121*, 2230-2291.

(5) Smith, M. D.; Crace, E. J.; Jaffe, A.; Karunadasa, H. I. The Diversity of Layered Halide Perovskites. *Annu. Rev. Mater. Res.* **2018**, *48*, 111-136.

(6) Ruddlesden, S. N.; Popper, P. The Compound $Sr_3Ti_2O_7$ and Its Structure . *Acta Crystallogr.* **1958**, *11* (1), 54-55.

(7) Ruddlesden, S. N.; Popper, P. New Compounds of the K_2NIF_4 Type . *Acta Crystallogr.* **1957**, *10* (8), 538-539.

(8) Smith, I. C.; Hoke, E. T.; Solis-Ibarra, D.; McGehee, M. D.; Karunadasa, H. I. A Layered Hybrid Perovskite Solar-Cell Absorber with Enhanced Moisture Stability. *Angew. Chemie* **2014**, *126* (42), 11414-11417.

(9) Stoumpos, C. C.; Cao, D. H.; Clark, D. J.; Young, J.; Rondinelli, J. M.; Jang, J. I.; Hupp, J. T.; Kanatzidis, M. G. Ruddlesden-Popper Hybrid Lead Iodide Perovskite 2D Homologous

Semiconductors. *Chem. Mater.* **2016**, *28* (8), 2852-2867.

(10) Mao, L.; Stoumpos, C. C.; Kanatzidis, M. G. Two-Dimensional Hybrid Halide Perovskites: Principles and Promises. *J. Am. Chem. Soc.* **2019**, *141* (3), 1171-1190.

(11) Ma, Z.; Li, F.; Sui, L.; Shi, Y.; Fu, R.; Yuan, K.; Xiao, G.; Zou, B. Tunable Color Temperatures and Emission Enhancement in 1D Halide Perovskites under High Pressure. *Adv. Opt. Mater.* **2020**, *8* (18), 1-7.

(12) Mao, L.; Wu, Y.; Stoumpos, C. C.; Traore, B.; Katan, C.; Even, J.; Wasielewski, M. R.; Kanatzidis, M. G. Tunable White-Light Emission in Single-Cation-Templated Three-Layered 2D Perovskites $(CH_3CH_2NH_3)_4Pb_3Br_{10-x}Cl_x$. *J. Am. Chem. Soc.* **2017**, *139* (34), 11956-11963.

(13) Luo, B.; Guo, Y.; Li, X.; Xiao, Y.; Huang, X.; Zhang, J. Z. Efficient Trap-Mediated Mn^{2+} Dopant Emission in Two Dimensional Single-Layered Perovskite $(CH_3CH_2NH_3)_2PbBr_4$. *J. Phys. Chem. C* **2019**, *123* (23), 14239-14245.

(14) Smith, M. D.; Jaffe, A.; Dohner, E. R.; Lindenberg, A. M.; Karunadasa, H. I. Structural Origins of Broadband Emission from Layered Pb-Br Hybrid Perovskites. *Chem. Sci.* **2017**, *8* (6), 4497-4504.

(15) Smith, M. D.; Connor, B. A.; Karunadasa, H. I. Tuning the Luminescence of Layered Halide Perovskites. *Chem. Rev.* **2019**, *119* (5), 3104-3139.

(16) Cortecchia, D.; Neutzner, S.; Kandada, A. R. S.; Mosconi, E.; Meggiolaro, D.; De Angelis, F.; Soci, C.; Petrozza, A. Broadband Emission in Two-Dimensional Hybrid Perovskites: The Role of Structural Deformation. *J. Am. Chem. Soc.* **2017**, *139* (1), 39-42.

(17) Hu, T.; Smith, M. D.; Dohner, E. R.; Sher, M. J.; Wu, X.; Trinh, M. T.; Fisher, A.; Corbett, J.; Zhu, X. Y.; Karunadasa, H. I.; Lindenberg, A.M. Mechanism for Broadband White-Light Emission from Two-Dimensional (110) Hybrid Perovskites. *J. Phys. Chem. Lett.* **2016**, *7* (12), 2258-2263.

(18) Decrescent, R. A.; Du, X.; Kennard, R. M.; Venkatesan, N. R.; Dahlman, C. J.; Chabinyc, M. L.; Schuller, J. A. Even-Parity Self-Trapped Excitons Lead to Magnetic Dipole Radiation in Two-Dimensional Lead Halide Perovskites. *ACS Nano* **2020**, *14* (7), 8958-8968.

(19) Li, S.; Luo, J.; Liu, J.; Tang, J. Self-Trapped Excitons in All-Inorganic Halide Perovskites: Fundamentals, Status, and Potential Applications. *J. Phys. Chem. Lett.* **2019**, *10* (8), 1999-2007.

(20) Li, J.; Wang, H.; Li, D. Self-Trapped Excitons in Two-Dimensional Perovskites. *Front. Optoelectron.* **2020**, *13* (3), 225-234.

(21) Wang, S.; Yao, Y.; Kong, J.; Zhao, S.; Sun, Z.; Wu, Z.; Li, L.; Luo, J. Highly Efficient White-Light Emission in a Polar Two-Dimensional Hybrid Perovskite. *Chem. Commun.* **2018**, *54* (32), 4053-4056.

(22) DeCrescent, R. A.; Venkatesan, N. R.; Dahlman, C. J.; Kennard, R. M.; Zhang, X.; Li, W.; Du, X.; Chabinyc, M. L.; Zia, R.; Schuller, J. A. Bright Magnetic Dipole Radiation from Two-Dimensional Lead-Halide Perovskites. *Sci. Adv.* **2020**, *6*, 1-11.

(23) Du, Q.; Zhu, C.; Yin, Z.; Na, G.; Cheng, C.; Han, Y.; Liu, N.; Niu, X.; Zhou, H.; Chen, H.; Zhang, L. ; Chen, Q. Stacking Effects on Electron-Phonon Coupling in Layered Hybrid

Perovskites via Microstrain Manipulation. *ACS Nano* **2020**, *14* (5), 5806-5817.

(24) Moral, R. F.; Germino, J. C.; Bonato, L. G.; Almeida, D. B.; Therézio, E. M.; Atvars, T. D. Z.; Stranks, S. D.; Nome, R. A.; Nogueira, A. F. Influence of the Vibrational Modes from the Organic Moieties in 2D Lead Halides on Excitonic Recombination and Phase Transition. *Adv. Opt. Mater.* **2020**, *8* (24), 1-8.

(25) Cortecchia, D.; Yin, J.; Bruno, A.; Lo, S. Z. A.; Gurzadyan, G. G.; Mhaisalkar, S.; Brédas, J. L.; Soci, C. Polaron Self-Localization in White-Light Emitting Hybrid Perovskites. *J. Mater. Chem. C* **2017**, *5* (11), 2771-2780.

(26) Kahmann, S.; Tekelenburg, E. K.; Duim, H.; Kamminga, M. E.; Loi, M. A. Extrinsic Nature of the Broad Photoluminescence in Lead Iodide-Based Ruddlesden-Popper Perovskites. *Nat. Commun.* **2020**, *11* (1), 1-8.

(27) Yu, J.; Kong, J.; Hao, W.; Guo, X.; He, H.; Leow, W. R.; Liu, Z.; Cai, P.; Qian, G.; Li, S.; Chen, X.; Chen, X. Broadband Extrinsic Self-Trapped Exciton Emission in Sn-Doped 2D Lead-Halide Perovskites. *Adv. Mater.* **2019**, *31* (7), 1-9.

(28) Kahmann, S.; Duim, H.; Fang, H.; Adjokatse, S.; Medina, R.; Pitaro, M.; Plochocka, P.; Loi, A. Photophysics of Two-Dimensional Perovskites - Learning from Metal Halide Substitution. *Arxiv* **2021**, 1-22.

(29) Gharibzadeh, S.; Hossain, I. M.; Fassl, P.; Nejand, B. A.; Abzieher, T.; Schultes, M.; Ahlswede, E.; Jackson, P.; Powalla, M.; Schäfer, S.; Rienäker, M.; Wietler, T.; Peibst, R.; Lemmer, U.; Richards, B. S.; Paetzold, U. W. 2D/3D Heterostructure for Semitransparent Perovskite Solar Cells with Engineered Bandgap Enables Efficiencies Exceeding 25% in

Four-Terminal Tandems with Silicon and CIGS. *Adv. Funct. Mater.* **2020**, *30* (19), 1909919.

(30) Gharibzadeh, S.; Abdollahi Nejand, B.; Jakoby, M.; Abzieher, T.; Hauschild, D.; Moghadamzadeh, S.; Schwenzer, J. A.; Brenner, P.; Schmager, R.; Haghighirad, A. A.; Weinhardt, L.; Lemmer, U.; Richards, B. S.; Howard, I. A.; Paetzold, U. W. Record Open-Circuit Voltage Wide-Bandgap Perovskite Solar Cells Utilizing 2D/3D Perovskite Heterostructure. *Adv. Energy Mater.* **2019**, *9* (21), 1803699.

(31) Sutanto, A. A.; Szostak, R.; Drigo, N.; Queloz, V. I. E.; Marchezi, P. E.; Germino, J. C.; Tolentino, H. C. N.; Nazeeruddin, M. K.; Nogueira, A. F.; Grancini, G. In Situ Analysis Reveals the Role of 2D Perovskite in Preventing Thermal-Induced Degradation in 2D/3D Perovskite Interfaces. *Nano Lett.* **2020**, *20* (5), 3992-3998.

(32) Grancini, G.; Roldán-Carmona, C.; Zimmermann, I.; Mosconi, E.; Lee, X.; Martineau, D.; Narbey, S.; Oswald, F.; De Angelis, F.; Graetzel, M.; Nazeeruddin, M. K. One-Year Stable Perovskite Solar Cells by 2D/3D Interface Engineering. *Nat. Commun.* **2017**, *8*, 1-8.

(33) Schlipf, J.; Hu, Y.; Pratap, S.; Bießmann, L.; Hohn, N.; Porcar, L.; Bein, T.; Docampo, P.; Müller-Buschbaum, P. Shedding Light on the Moisture Stability of 3D/2D Hybrid Perovskite Heterojunction Thin Films. *ACS Appl. Energy Mater.* **2019**, *2* (2), 1011-1018.

(34) Yuan, M.; Quan, L. N.; Comin, R.; Walters, G.; Sabatini, R.; Voznyy, O.; Hoogland, S.; Zhao, Y.; Beauregard, E. M.; Kanjanaboos, P.; Lu, Z.; Kim, D. H.; Sargent, E. H. Perovskite Energy Funnels for Efficient Light-Emitting Diodes. *Nat. Nanotechnol.* **2016**, *11* (10), 872-877.

(35) Li, T.; Zeidell, A. M.; Findik, G.; Dunlap-Shohl, W. A.; Euvrard, J.; Gundogdu, K.; Jurchescu, O. D.; Mitzi, D. B. Phase-Pure Hybrid Layered Lead Iodide Perovskite Films Based on a Two-Step Melt-Processing Approach. *Chem. Mater.* **2019**, *31* (11), 4267-4274.

(36) Liang, C.; Gu, H.; Xia, Y.; Wang, Z.; Liu, X.; Xia, J.; Zuo, S.; Hu, Y.; Gao, X.; Hui, W.; Chao, L. ; Niu, T.; Fang, M.; Lu, H.; Dong, H.; Yu, H.; Chen, S.; Ran, X.; Song, L.; Li, B.; Zhang, J.; Peng, Y.; Shao, G.; Wang, J.; Chen, Y.; Xing, G.; Huang, W. Two-Dimensional Ruddlesden–Popper Layered Perovskite Solar Cells Based on Phase-Pure Thin Films. *Nat. Energy* **2020**, *6*, 38-4.

(37) Rolston, N.; Bush, K. A.; Printz, A. D.; Gold-Parker, A.; Ding, Y.; Toney, M. F.; McGehee, M. D.; Dauskardt, R. H. Engineering Stress in Perovskite Solar Cells to Improve Stability. *Adv. Energy Mater.* **2018**, *8* (29), 1-7.

(38) Bush, K. A.; Rolston, N.; Gold-Parker, A.; Manzoor, S.; Hausele, J.; Yu, Z. J.; Raiford, J. A.; Cheacharoen, R.; Holman, Z. C.; Toney, M. F.; Dauskardt, R. H.; McGehee, M. D. Controlling Thin-Film Stress and Wrinkling during Perovskite Film Formation. *ACS Energy Lett.* **2018**, *3* (6), 1225-1232.

(39) Kennard, R. M.; Dahlman, C. J.; DeCrescent, R. A.; Schuller, J. A.; Mukherjee, K.; Seshadri, R.; Chabinyc, M. L. Ferroelastic Hysteresis in Thin Films of Methylammonium Lead Iodide. *Chem. Mater.* **2021**, *33*, 298-309.

(40) Steele, J. A.; Jin, H.; Dovgaliuk, I.; Berger, R. F.; Braeckevelt, T.; Yuan, H.; Martin, C.; Solano, E.; Lejaeghere, K.; Rogge, S. M. J.; Notebaert, C.; Wouter, V.; Janssen, K. P. F.; Goderis, B.; Debroye, E.; Wang, Y.; Dong, Y.; Ma, D.; Saidaminov, M.; Tan, H.; Lu, Z,; Dyadkin, V.; Chernyshov, D.; Speybroeck, V. V.; Sargent, E. H.; Hofkens, J.; Roeffaers,

M. B. J. Thermal Unequilibrium of Strained Black $CsPbI_3$ Thin Films. *Science* **2019**, *365(6454)*, 679-684.

(41) Zhu, C.; Niu, X.; Fu, Y.; Li, N.; Hu, C.; Chen, Y.; He, X.; Na, G.; Liu, P.; Zai, H.; Ge, Y.; Lu, Y.; Ke, X.; Bai, Y.; Yang, S.; Chen, P.; Li, Y.; Sui, M.; Zhang, L.; Zhou, H.; Chen, Q. Strain Engineering in Perovskite Solar Cells and Its Impacts on Carrier Dynamics. *Nat. Commun.* **2019**, *10* (1), 1-11.

(42) Jones, T. W.; Osherov, A.; Alsari, M.; Sponseller, M.; Duck, B. C.; Jung, Y.-K.; Settens, C.; Niroui, F.; Brenes, R.; Stan, C. V.; Li, Y.; Abdi-Jalebi, M.; Tamura, N.; Macdonald, J. E.; Burghammer, M.; Friend, R. H.; Bulović, V.; Walsh, A.; Wilson, G. J.; Lilliu, S.; and Stranks, S. D. Lattice strain causes non-radiative losses in halide perovskites. *Energy & Environmental Science*, **2019**, *12(2*), 596-606.

(43) Tu, Q.; Spanopoulos, I.; Hao, S.; Wolverton, C.; Kanatzidis, M. G.; Shekhawat, G. S.; Dravid, V. P. Probing Strain-Induced Band Gap Modulation in 2D Hybrid Organic-Inorganic Perovskites. *ACS Energy Lett.* **2019**, *4* (3), 796-802.

(44) Zhou, M.; Fei, C.; Sarmiento, J. S.; Wang, H. Manipulating the Phase Distributions and Carrier Transfers in Hybrid Quasi-Two-Dimensional Perovskite Films. *Sol. RRL* **2019**, *3* (4), 1-9.

(45) Venkatesan, N. R.; Kennard, R. M.; DeCrescent, R. A.; Nakayama, H.; Dahlman, C. J.; Perry, E. E.; Schuller, J.; Chabinyc, M. L. Phase Intergrowth and Structural Defects in Organic Metal Halide Ruddlesden-Popper Thin Films. *Chem. Mater.* **2018**, *30*, 8615-8623.

(46) Tan, W. L.; Cheng, Y. B.; McNeill, C. R. Direct Assessment of Structural Order and

Evidence for Stacking Faults in Layered Hybrid Perovskite Films from X-Ray Scattering Measurements. *J. Mater. Chem. A* **2020**, *8* (25), 12790-12798.

(47) Blancon, J. C.; Tsai, H.; Nie, W.; Stoumpos, C. C.; Pedesseau, L.; Katan, C.; Kepenekian, M.; Soe, C. M. M.; Appavoo, K.; Sfeir, M. Y.; Tretiak, S.; Ajayan, P. M.; Kanatzidis, M. G.; Even, J.; Crochet, J. J.; Mohite, A. D. Extremely Efficient Internal Exciton Dissociation through Edge States in Layered 2D Perovskites. *Science* **2017**, *355* (6331), 1288-1292.

(48) Dahlman, C. J.; Decrescent, R. A.; Venkatesan, N. R.; Kennard, R. M.; Wu, G.; Everest, M. A.; Schuller, J. A.; Chabinyc, M. L. Controlling Solvate Intermediate Growth for Phase-Pure Organic Lead Iodide Ruddlesden-Popper $(C_4H_9NH_3)_2(CH_3NH_3)_{n-1}Pb_nI_{3n+1}$ Perovskite Thin Films. *Chem. Mater.* **2019**, *31* (15), 5832-5844.

(49) Quintero-Bermudez, R.; Gold-Parker, A.; Proppe, A. H.; Munir, R.; Yang, Z.; Kelley, S. O.; Amassian, A.; Toney, M. F.; Sargent, E. H. Compositional and Orientational Control in Metal Halide Perovskites of Reduced Dimensionality. *Nat. Mater.* **2018**, *17* (10), 900-907.

(50) Hoffman, J. M.; Strzalka, J.; Flanders, N. C.; Hadar, I.; Cuthriell, S. A.; Zhang, Q.; Schaller, R. D.; Dichtel, W. R.; Chen, L. X.; Kanatzidis, M. G. In Situ Grazing-Incidence Wide-Angle Scattering Reveals Mechanisms for Phase Distribution and Disorientation in 2D Halide Perovskite Films. *Adv. Mater.* **2020**, *32* (33), 1-8.

(51) Shi, E.; Deng, S.; Yuan, B.; Gao, Y.; Akriti; Yuan, L.; Davis, C. S.; Zemlyanov, D.; Yu, Y.; Huang, L.; Dou, L. Extrinsic and Dynamic Edge States of Two-Dimensional Lead Halide Perovskites. *ACS Nano* **2019**, *13* (2), 1635-1644.

(52) Williams, O. F.; Guo, Z.; Hu, J.; Yan, L.; You, W.; Moran, A. M. Energy Transfer

Mechanisms in Layered 2D Perovskites. *J. Chem. Phys.* **2018**, *148* (13), 134706, 1-16.

(53) Yantara, N.; Bruno, A.; Iqbal, A.; Jamaludin, N. F.; Soci, C.; Mhaisalkar, S.; Mathews, N. Designing Efficient Energy Funneling Kinetics in Ruddlesden-Popper Perovskites for High-Performance Light-Emitting Diodes. *Adv. Mater.* **2018**, *30* (33), 1-7.

(54) Ren, Z.; Li, L.; Yu, J.; Ma, R.; Xiao, X.; Chen, R.; Wang, K.; Sun, X. W.; Yin, W. J.; Choy, W. C. H. Simultaneous Low-Order Phase Suppression and Defect Passivation for Efficient and Stable Blue Light-Emitting Diodes. *ACS Energy Lett.* **2020**, *5* (8), 2569-2579.

(55) Mao, P.; Zhuang, J.; Wei, Y.; Chen, N.; Luan, Y.; Wang, J. Origin and Suppression of the Graded Phase Distribution in Ruddlesden-Popper Perovskite Films for Photovoltaic Application. *Sol. RRL* **2019**, *3* (4), 1-8.

(56) Luo, S. Q.; Wang, J. F.; Yang, B.; Yuan, Y. B. Recent Advances in Controlling the Crystallization of Two-Dimensional Perovskites for Optoelectronic Device. *Front. Phys.* **2019**, *14* (5), 53401, 1-11.

(57) Han, Y.; Park, S.; Kim, C.; Lee, M.; Hwang, I. Phase Control of Quasi-2D Perovskites and Improved Light-Emitting Performance by Excess Organic Cations and Nanoparticle Intercalation. *Nanoscale* **2019**, *11* (8), 3546-3556.

(58) Liu, P.; Han, N.; Wang, W.; Ran, R.; Zhou, W.; Shao, Z. High-Quality Ruddlesden–Popper Perovskite Film Formation for High-Performance Perovskite Solar Cells. *Adv. Mater.* **2021**, 33(10), 2002582.

(59) Yan, L.; Hu, J.; Guo, Z.; Chen, H.; Toney, M. F.; Moran, A. M.; You, W. General Post-Annealing Method Enables High-Efficiency Two-Dimensional Perovskite Solar Cells. *ACS*

Appl. Mater. Interfaces **2018**, *10* (39), 33187-33197.

(60) Chen, A. Z.; Shiu, M.; Deng, X.; Mahmoud, M.; Zhang, D.; Foley, B. J.; Lee, S. H.; Giri, G.; Choi, J. J. Understanding the Formation of Vertical Orientation in Two-Dimensional Metal Halide Perovskite Thin Films. *Chem. Mater.* **2019**, *31* (4), 1336-1343.

(61) Wang, R.; Tong, Y.; Manzi, A.; Wang, K.; Fu, Z.; Kentzinger, E.; Feldmann, J.; Urban, A. S.; Müller-Buschbaum, P.; Frielinghaus, H. Preferential Orientation of Crystals Induced by Incorporation of Organic Ligands in Mixed-Dimensional Hybrid Perovskite Films. *Adv. Opt. Mater.* **2018**, *6* (6), 1-9.

(62) GIXA Calculator for Penetration Depth (and Optical Properties) for X-rays https://gixa.ati.tuwien.ac.at/tools/penetrationdepth.xhtml (accessed Nov 9, 2020).

(63) Venkatesan, N. R.; Labram, J. G.; Chabinyc, M. L. Charge-Carrier Dynamics and Crystalline Texture of Layered Ruddlesden-Popper Hybrid Lead Iodide Perovskite Thin Films. *ACS Energy Lett.* **2018**, *3* (2), 380-386.

(64) Resel, R.; Bainschab, M.; Pichler, A.; DIngemans, T.; Simbrunner, C.; Stangl, J.; Salzmann, I. Multiple Scattering in Grazing-Incidence X-Ray Diffraction: Impact on Lattice-Constant Determination in Thin Films. *J. Synchrotron Radiat.* **2016**, *23* (3), 729-734.

(65) Vandewal, K.; Albrecht, S.; Hoke, E. T.; Graham, K. R.; Widmer, J.; Douglas, J. D.; Schubert, M.; Mateker, W. R.; Bloking, J. T.; Burkhard, G. F.; Sellinger; A.; Fréchet, J. M. J.; Amassian, A.; Riede, M. K.; McGehee, M. D.; Neher, D.; Salleo, A. Efficient Charge Generation by Relaxed Charge-Transfer States at Organic Interfaces. *Nat. Mater.* **2014**, *13* (1), 63-68.

(66) Kieslich, G.; Sun, S.; Cheetham, A. K. An Extended Tolerance Factor Approach for Organic-Inorganic Perovskites. *Chem. Sci.* **2015**, *6* (6), 3430-3433.

(67) Becker, M.; Klüner, T.; Wark, M. Formation of Hybrid ABX_3 Perovskite Compounds for Solar Cell Application: First-Principles Calculations of Effective Ionic Radii and Determination of Tolerance Factors. *Dalt. Trans.* **2017**, *46* (11), 3500-3509.

(68) Yoon, S. J.; Stamplecoskie, K. G.; Kamat, P. V. How Lead Halide Complex Chemistry Dictates the Composition of Mixed Halide Perovskites. *J. Phys. Chem. Lett.* **2016**, *7* (7), 1368-1373.

(69) Proppe, A. H.; Quintero-Bermudez, R.; Tan, H.; Voznyy, O.; Kelley, S. O.; Sargent, E. H. Synthetic Control over Quantum Well Width Distribution and Carrier Migration in Low-Dimensional Perovskite Photovoltaics. *J. Am. Chem. Soc.* **2018**, *140* (8), 2890-2896.

(70) Mooney, J.; Kambhampati, P. Get the Basics Right: Jacobian Conversion of Wavelength and Energy Scales for Quantitative Analysis of Emission Spectra. *J. Phys. Chem. Lett.* **2013**, *4* (19), 3316-3318.

(71) Schotz, K.; Abdelrahman, M. A.; Peng, W.; Seeberger, D.; Gujar, T. P.; Thelakkat, M.; Kohler, A.; Huettner, S.; Bakr, O. M.; Shankar, K.; Panzer, F. Double Peak Emission in Lead Halide Perovskites by Self-Absorption. *J. Mater. Chem. C* **2020**, *8*, 2289-2300.

(72) Messerschmidt, S.; Krampf, A.; Freytag, F.; Imlau, M.; Vittadello, L.; Bazzan, M.; Corradi, G. The Role of Self-Trapped Excitons in Polaronic Recombination Processes in Lithium Niobate. *J. Phys. Condens. Matter* **2019**, *31* (6), 065701.

(73) Gandhi, A. C.; Yeoh, W. S.; Wu, M. A.; Liao, C. H.; Chiu, D. Y.; Yeh, W. L.; Huang, Y.

L. New Insights into the Role of Weak Electron–Phonon Coupling in Nanostructured ZnO Thin Films. *Nanomaterials* **2018**, *8* (8), 632.

(74) Seong, M. J.; Mićić, O. I.; Nozik, A. J.; Mascarenhas, A.; Cheong, H. M. Size-Dependent Raman Study of InP Quantum Dots. *Appl. Phys. Lett.* **2003**, *82* (2), 185-187.

(75) Li, Q.; Chen, Z.; Li, M.; Xu, B.; Han, J.; Luo, Z.; Tan, L.; Xia, Z.; Quan, Z. Pressure-Engineered Photoluminescence Tuning in Zero-Dimensional Lead Bromide Trimer Clusters. *Angew. Chemie - Int. Ed.* **2021**, *60* (5), 2583-2587.

(76) Tu, Q.; Spanopoulos, I.; Hao, S.; Wolverton, C.; Kanatzidis, M. G.; Shekhawat, G. S.; Dravid, V. P. Out-of-Plane Mechanical Properties of 2D Hybrid Organic-Inorganic Perovskites by Nanoindentation. *ACS Appl. Mater. Interfaces* **2018**, *10* (26), 22167-22173.

(77) Feng, J. Mechanical Properties of Hybrid Organic-Inorganic $CH_3NH_3BX_3$ (B = Sn, Pb; X = Br, I) Perovskites for Solar Cell Absorbers. *APL Mater.* **2014**, *2* (8), 081801.

(78) Mao, W.; Zheng, J.; Zhang, Y.; Chesman, A. S. R.; Ou, Q.; Hicks, J.; Li, F.; Wang, Z.; Graystone, B.; Bell, T. D. M.; Rothmann, M. U.; Duffy, N. W.; Spiccia, L.; Cheng, Y.; Bao, Q.; Bach, U. Controlled Growth of Monocrystalline Organo-Lead Halide Perovskite and Its Application in Photonic Devices. *Angew. Chemie - Int. Ed.* **2017**, *56* (41), 12486-12491.

(79) Gholipour, S.; Ali, A. M.; Correa-Baena, J. P.; Turren-Cruz, S. H.; Tajabadi, F.; Tress, W.; Taghavinia, N.; Grätzel, M.; Abate, A.; De Angelis, F.; Gaggioli, C. A. ; Mosconi, E. ; Hagfeldt, A. ; Saliba, M. Globularity-Selected Large Molecules for a New Generation of Multication Perovskites. *Adv. Mater.* **2017**, *29* (38), 1-9.

(80) Mittal, M.; Jana, A.; Sarkar, S.; Mahadevan, P.; Sapra, S. Size of the Organic Cation Tunes

the Band Gap of Colloidal Organolead Bromide Perovskite Nanocrystals. *J. Phys. Chem. Lett.* **2016**, *7* (16), 3270-3277.

(81) Fu, Y.; Hautzinger, M. P.; Luo, Z.; Wang, F.; Pan, D.; Aristov, M. M.; Guzei, I. A.; Pan, A.; Zhu, X.; Jin, S. Incorporating Large A Cations into Lead Iodide Perovskite Cages: Relaxed Goldschmidt Tolerance Factor and Impact on Exciton-Phonon Interaction. *ACS Cent. Sci.* **2019**, *5* (8), 1377-1386.

(82) Goldschmidt, V. V. Die Gesetze Der Krystallochemie. *Naturwissenschaften* **1926**, *14*, 477-485.

TOC GRAPHICS